

Porosity-Permeability Relationships in Mudstone from Pore-Scale Fluid Flow Simulations using the Lattice Boltzmann Method

Harsh Biren Vora¹, Brandon Dugan²

¹Department of Earth, Environment and Planetary Sciences, Rice University, Houston, TX 77005

²Department of Geophysics, Colorado School of Mines, Golden, CO 80401

Corresponding Author: Harsh Biren Vora (hv6@rice.edu)

Key Points:

- We develop a model to predict mudstone permeability from clay platelet geometry using lattice Boltzmann simulations
- Modeled porosity-permeability predictions match experimental observations from synthetic and natural mudstones
- Our model can simulate mudstone permeability response to compaction and to fluid injection using porosity and clay mineralogy

Abstract

We model mudstone permeability during consolidation and during fluid injection by simulating porous media flow using the lattice Boltzmann method. We define the mudstone structure using clay platelet thickness, aspect ratio, orientation and pore widths. Over the representative range of clay platelet lengths (0.1–3 μm), aspect ratios (length/thickness=20-50) and porosities (ϕ =0.07–0.80) our permeability results match mudstone datasets well. Homogenous smectite and kaolinite models document log-linear decline in vertical permeability from $8.31 \times 10^{-15} \text{ m}^2$ – $6.84 \times 10^{-17} \text{ m}^2$ at ϕ =0.73-0.80 to $6.33 \times 10^{-19} \text{ m}^2$ – $1.30 \times 10^{-23} \text{ m}^2$ at ϕ =0.07-0.16, showing good correlation with experimental trends (R^2 =0.42 and 0.56). We then test our methodology to predict the permeability in natural mudstones consisting of smectite, illite and chlorite grains. Over ϕ =0.32-0.58, the permeability trends of two models replicating the mineralogical composition of natural mudstones match experimental datasets well (R^2 =0.78 and 0.74). We extend our methodology to evaluate how vertical mudstone permeability might evolve during microfracture network growth or macrofracture propagation upon fluid injection. Fluid injection causing a porosity increase from 0.07 to 0.57 results in a permeability increase from $1.02 \times 10^{-20} \text{ m}^2$ to $9.59 \times 10^{-15} \text{ m}^2$ for growth of a microfracture network, and from $1.02 \times 10^{-20} \text{ m}^2$ to $3.85 \times 10^{-14} \text{ m}^2$ for macrofracture propagation. Our results suggest that a distributed microfracture network results in greater permeability during initial fluid injection (ϕ =0.07-0.36), whereas a macrofracture yields greater permeability once it is wide enough to conduct the bulk of fluid flux (ϕ =0.36-0.57). Our modeling approach provides a simple means to estimate permeability during burial and compaction or fluid injection based on knowledge of porosity and mineralogy.

1. Introduction

Mudstone comprises 60-70% of sedimentary basin fill. During burial to 5 km, mudstone porosity (ϕ) decreases from 0.9 to 0.05, which coincides with decline in permeability (k) of up to 10 orders of magnitude [Neuzil, 1994]. These variations in permeability are important for several geological applications such as pore pressure development [Lou and Vasseur, 1992], continental slope stability

[Dugan and Flemings, 2000], hydrocarbon retention [England et al., 1987], and shale gas production [Soeder, 1988]. Accurate prediction of mudstone permeability, however, remains challenging due to the factors influencing permeability such as grain dimension [Schwartz and Banavar, 1989], platelet orientation [Clennell et al., 1999], and pore geometry [Bowers and Katsube, 2002]. Clay minerals and their dimensions are often suggested as primary controls on mudstone permeability [Olsen, 1962; Dewhurst et al., 1996]. Clay platelet length ranges from 0.1 μm to 10 μm [Mondol et al., 2007] and platelets have aspect ratios (length/thickness) of 1 to 100 [Santamarina et al., 2002]. This large variation in grain dimension is suggested as the dominant controlling factor in mudstone permeability spanning 3-4 orders of magnitude for a single porosity value [Dewhurst et al., 1999a; Mondol et al., 2008].

Several models have been proposed to explain mudstone permeability. Many models assume a log-linear relationship between permeability and porosity [Rose, 1945, Nagaraj et al., 1994; Neuzil, 1994], but fail to explain the observed range of mudstone permeability for a given porosity [Yang and Aplin, 2007]. Another model used to predict mudstone permeability is the Kozeny-Carman model [Kozeny, 1927; Carman, 1937], which requires information on tortuosity, pore factor, specific pore surface area, and pore volume. While the Kozeny-Carman relationship can predict the permeability of unconsolidated mudstones with reasonable accuracy [Chapuis and Aubertin, 2003], various studies document prediction errors of several orders of magnitude [Yang and Aplin, 1998; Dewhurst et al., 1999a, b]. In other work, Yang and Aplin [2007] use pore size distribution measurements to develop an empirical power law relationship between mudstone permeability and mean pore throat radius. Thus, while several models exist to predict mudstone permeability, their application requires knowledge of pore size and tortuosity, and do not directly account for the effect of clay platelet geometry.

To improve mudstone permeability characterization, we develop a model that directly includes clay platelet geometry. We employ a three-dimensional, pore-scale model using clay platelet dimensions, pore throat widths, platelet orientation, and porosity. We use this to evaluate the impacts of clay platelet geometry and porosity loss on permeability during burial. We estimate permeability in mudstones of

homogenous mineralogy from lattice Boltzman simulations of water flow through mudstone pore structures and validate our results against compilation of experimental and field datasets. We employ our modeling approach to predict porosity-permeability relationships in natural mudstones of heterogenous clay mineralogy and compare our results against experimental datasets. Finally, we extend our model to fluid injection by modifying pore structure to assess how permeability changes with growth of a microfracture network and with propagation of a macrofracture. Thus, with information on clay mineralogy, clay content, and porosity, our new approach can help estimate permeability in mudstones subjected to anthropogenic fluid injection from wastewater disposal, hydraulic fracturing, and carbon sequestration.

2. Methods

2.1. Initial Mudstone Pore Structure

We build our mudstone models from cuboidal platelets arranged in bedding layers, with each platelet oriented at an angle θ from the horizontal [Fig. 1a]. Each clay platelet has a thickness (β) and a length and width ($m\beta$), where m is the aspect ratio of the clay platelets. Pore space between particles is defined by intrabed pores of a finite width (ε) and by interbed pores, each of length and width (λ) [Fig. 1a]. To analyze mineralogy-specific porosity-permeability behavior of mudstones, we initially design three homogenous mudstone models using (1) kaolinite particles, (2) smectite particles, and (3) clay particles of intermediate size.

In general, kaolinite particles have a length of 1- 10 μm and aspect ratios up to 25, whereas smectite particles have a length up to 0.1 μm and aspect ratios up to 100 [Mitchell and Soga, 2005]. We simulate kaolinite mudstone starting with $\phi=0.76$ ($m = 20$; $m\beta = 3 \mu\text{m}$; $\varepsilon = \lambda = 360 \text{ nm}$). We simulate smectite mudstone starting with $\phi=0.80$ ($m = 50$; $m\beta = 0.1 \mu\text{m}$; $\varepsilon = \lambda = 9 \text{ nm}$). We simulate the intermediate mudstone starting with $\phi=0.73$ ($m = 35$; $m\beta = 2 \mu\text{m}$; $\varepsilon = \lambda = 137 \text{ nm}$). Our initial mudstone porosity of 0.73-0.80 lies within range of porosity for near-seafloor mud [Daigle and Screatton, 2015; Cook and

Sawyer, 2015]. Our initial pore widths of 9-360 nm are consistent with pore sizes determined from scanning electron microscopy and mercury intrusion porosimetry analyses of unconsolidated marine mudstones (1-5000 nm) [Heath, 2010], siliceous mudstones (5-750 nm) [Loucks et al., 2009], and London Clay (10-500 nm) [Dewhurst et al., 1999b].

Mineral grains are oriented randomly at deposition [Bennett et al., 1989]. In contrast, clay platelets in our model are oriented at the same angle with respect to the horizontal, θ [Fig. 1a]. Daigle and Dugan [2011] show that a porous medium with uniformly distributed grain orientations between θ_1 and θ_2 can be represented using the mean orientation angle (θ) of all grains in the matrix ($\theta = (\theta_1 + \theta_2)/2$). Clay platelet orientations can range between 0° to 90° from horizontal at deposition ($\theta_1 = 0^\circ$, $\theta_2 = 90^\circ$, $\theta = 45^\circ$) [Deamer and Kodama, 1990], therefore, we implement an initial platelet orientation of $\theta = 45^\circ$ in our mudstone models.

2.2. Lattice Boltzmann Simulations

We use the open source code OpenLB [Latt, 2008] to simulate water flow through mudstone using the lattice Boltzmann method. We choose the lattice Boltzmann method because it has been used successfully to predict the permeability of sandstones [Bosl et al., 1998], to estimate sandstone permeability from thin sections [Keehm et al., 2004], and to model the development of permeability anisotropy in mudstones [Daigle and Dugan, 2011]. Lattice Boltzmann simulations of flow yield fluid flux (q) for an applied pressure differential (ΔP); conversions between lattice Boltzmann units and SI units are made using guidelines described by Chukwodie [2011]. For all simulations, we apply a constant pressure differential (ΔP) of 88×10^3 Pa across the model domain in the direction of flow and implement the particle bounce-back scheme [Bouzidi et al., 2001] along the orthogonal edges. Water (dynamic viscosity, $\mu_w = 8.9 \times 10^{-4}$ Pa·s; density, $\rho_w = 1000$ kg/m³) is used as the permeating fluid. By applying ΔP in different directions, we determine vertical water flux (q_v), horizontal water flux in the plane of platelet rotation (q_{h1}) and horizontal water flux orthogonal to plane of platelet rotation (q_{h2}). In our study, we focus on horizontal water flux in the plane of platelet rotation (q_{h1}), hereafter referred to as q_h [Fig. 1a].

2.3. Calculation of Permeability and Tortuosity

We rearrange Darcy's law to calculate permeability (k) from our simulation results,

$$k = \mu_w * q * L / \Delta P \quad (1)$$

where k is permeability (m^2) and L is the length (m) over which pressure differential is applied. Vertical permeability (k_v) is calculated using water flux in the vertical direction (q_v) and horizontal permeability (k_h) is calculated using water flux in the horizontal direction (q_h). Permeability anisotropy is calculated as k_h/k_v . To ensure the applicability of Darcy's Law, we maintain Reynolds Number ($Re = (\rho_w * q * m \beta) / \mu_w$) less than 10 for all simulations.

We supplement permeability predictions with calculations of tortuosity (τ) to validate our methodology.

We adapt the approach of Nabovati and Sousa [2007] to calculate vertical tortuosity (τ_v) and horizontal tortuosity (τ_h),

$$\tau_v = \frac{\sqrt{q_v^2 + 2 q_h^2}}{q_v}, \quad (2)$$

$$\tau_h = \frac{\sqrt{q_v^2 + 2 q_h^2}}{q_h}. \quad (3)$$

2.4. Mudstone Compaction

We simulate compaction through simultaneous decline in mudstone porosity and grain orientation [Fig. 1b]. Porosity loss during compaction is simulated through imposed, step-wise reduction of intrabed and interbed pore widths [Table S1]. After compaction our modeled mudstones have pore widths of 1-40 nm, which is consistent with pore throat diameters in compacted mudstones measured by X-ray diffraction and nitrogen gas-adsorption [Katsube and Williamson, 1994; Kuila and Prasad, 2012].

Natural and experimental mudstone compaction document a decline in range of observed grain orientations [Day-Stirrat et al., 2012] and an increase in horizontal bedding character [Aplin et al., 2006]. During compaction we assume a decline in θ_2 from 90° to 0° and $\theta_1=0^\circ$. We implement a compaction

orientation function in our mudstone models through the prescribed decline in representative platelet orientation ($\theta = (\theta_1 + \theta_2)/2$) from 45° to 0° [Table S1]. In general, the modeled compaction orientation function replicates the increase in horizontal bedding character during compaction in mudstones, observed during natural and experimental compaction. We simulate faster decline in platelet orientation angle at high porosity states in our models [Table S1], consistent with experimental mudstone compaction [Dewhurst et al., 1999a]. Vertical and horizontal permeability is calculated during the step-wise compaction of mudstone models [Table S1].

3. Compaction Model Results

In our kaolinite compaction model, k_v decreases from $8.31 \times 10^{-15} \text{ m}^2$ at $\phi = 0.76$ to $6.33 \times 10^{-19} \text{ m}^2$ at $\phi = 0.14$ [Fig. 2], following a log-linear trend ($R^2 = 0.99$),

$$\log(k_v^{kaolinite}) = 6.48 \phi - 18.86 . \quad (4)$$

Simultaneously, k_h decreases from $1.01 \times 10^{-14} \text{ m}^2$ to $1.43 \times 10^{-17} \text{ m}^2$ [Table S1] and k_h/k_v increases from 1.32 to 22.6 [Fig. 3]. The reduction in vertical permeability during compaction is accompanied by an increase in vertical tortuosity from 1.02 to 2.06 [Fig. S1a] and a decrease in horizontal tortuosity from 6.56 to 1.62 [Table S1].

In our smectite compaction model, k_v decreases from $6.48 \times 10^{-17} \text{ m}^2$ at $\phi = 0.80$ to $1.30 \times 10^{-23} \text{ m}^2$ at $\phi = 0.16$ [Fig. 2], following a log-linear trend ($R^2 = 0.99$),

$$\log(k_v^{smectite}) = 10.59 \phi - 24.44 . \quad (5)$$

Simultaneously, k_h decreases from $1.33 \times 10^{-16} \text{ m}^2$ to $9.35 \times 10^{-22} \text{ m}^2$ [Table S1] and k_h/k_v increases from 1.94 to 71.9 [Fig. 3]. The reduction in vertical permeability during compaction is accompanied by an increase in vertical tortuosity from 1.01 to 2.56 [Fig. S1a] and a decrease in horizontal tortuosity from 8.64 to 1.54 [Table S1].

In our intermediate mudstone compaction model, k_v decreases from $6.10 \times 10^{-16} \text{ m}^2$ at $\phi = 0.73$ to $1.02 \times 10^{-20} \text{ m}^2$ at $\phi = 0.07$ [Fig. 2], following a log-linear trend ($R^2 = 0.98$),

$$\log(k_v^{int}) = 6.73 \phi - 20.16 . \quad (6)$$

Simultaneously, k_h decreases from $1.11 \times 10^{-15} \text{ m}^2$ to $4.68 \times 10^{-19} \text{ m}^2$ [Table S1] and k_h/k_v increases from 1.82 to 45.6 [Fig. 3]. The reduction in vertical permeability during compaction is accompanied by an increase in vertical tortuosity from 1.02 to 2.20 [Fig. S1a] and a decrease in horizontal tortuosity from 8.06 to 1.59 [Table S1].

The modeled decreases in k_v and k_h during compaction are due to a reduction of pore throat widths. Greater values of k_h compared to k_v occur as interbed pores provide greater continuity in pathways for horizontal fluid flow, while clay platelets create a more tortuous pathway for vertical flow. Vertical tortuosity increases while horizontal tortuosity decreases during compaction which amplifies permeability anisotropy [Fig. 3].

4. Discussion

4.1. Validation of Porosity-Permeability Models

We compare our modeled porosity-permeability relationships with experimental and field mudstone data [Mondol et al., 2008, Neuzil, 1994]. Our kaolinite and smectite models [Eq. 4,5] show good correlation (R^2 of 0.42 and 0.56) with experimental data [Fig. 2]. The modeled porosity-permeability relationships lie within range of experimental and natural mudstone datasets, and the intermediate mudstone model [Eq. 6] depicts the bulk compaction-permeability behavior of mudstones [Fig. 2]. These results validate our modeling approach over representative range of grain sizes (0.1-3 μm), aspect ratios (20-50), grain orientations (45° - 0°), and porosity (0.80-0.07).

Existing experimental and modeled values for mudstone tortuosity range from 1 to 3.5 as porosity decreases from 0.9 to 0.1 [Iversen and Jørgensen, 1993; Boudreau and Meysmann, 2006]. We calculate values of vertical tortuosity of 1.01-2.56 during compaction [Table S1], which lies within range of reported tortuosity values. The increase in τ_v during compaction is accompanied by a decline in τ_h [Table S1], which is consistent with experimental observations [Dewhurst et al., 1999a]. This provides additional validation of our model approach.

During compaction, our model results also document increasing permeability anisotropy from 1.32-1.94 at $\phi=0.72 - 0.80$ to 22.6 – 71.9 at $\phi=0.07 - 0.16$ [Fig. 3]. Experimentally determined values of anisotropy in mudstones document an increase from 1.5 to 40 during compaction [Arch and Maltman, 1990; Bhandari et al., 2015; Yang and Aplin, 2007]. Over $\phi=0.80 - 0.15$, predictions of k_h/k_v from our mudstone models lie within range of experimentally documented mudstone anisotropy values [Fig. 3]. At porosity less than 0.15, when $\theta=0^\circ$ in our models, our smectite and intermediate mudstone models predict k_h/k_v of 71.9 and 45.6, which exceeds the range of experimental mudstone anisotropy. This overprediction of k_h/k_v is due to the simplified horizontal layering of platelets when $\theta=0^\circ$. This results in horizontally continuous interbed pores and overprediction of k_h , resulting in higher anisotropy values. While these k_h/k_v values lie outside experimentally observed anisotropy values, several field-scale studies infer $k_h/k_v > 100$ based on basin-scale models [Freeze and Cherry, 1979; Garven and Freeze, 1984; Bolton et al., 2000; Day-Stirrat et al., 2008]. Our models suggest that high bedding character resulting in lateral continuity of interbed pores could explain the larger k_h/k_v values inferred from analysis of natural flow systems. Thus, for compaction from $\phi=0.80$ to 0.07, our methodology of simulating flow through modeled mudstone pore structures provides good estimates of permeability, permeability anisotropy, and tortuosity for homogenous mudstones. While our results from homogenous mudstones lie within range of observations from natural mudstones [Fig. 2], they do not describe the porosity-permeability character of mudstones of heterogenous clay mineralogy, so we assess our validated methodology against data from natural mudstones of known and heterogeneous clay mineralogy.

4.2. Permeability Prediction in Natural Mudstones

We test our modeling approach against the porosity-permeability character of two natural mudstones from the Ursa Basin, Gulf of Mexico [Sawyer et al., 2009]. Sample 1324C-1H-1 has a clay mineral weight fraction of 70.4%, consisting dominantly of smectite and illite [Table 1]. Sample 1324B-7H-7 has a clay mineral weight fraction of 68.9%, consisting dominantly of smectite, illite, and chlorite [Table 1]. To

simulate the porosity-permeability behavior of these two samples, we model permeability with clay platelets of heterogenous dimensions.

We adapt our model to include mineral weight fractions of smectite, illite, and chlorite to simulate the mudstone pore structures of samples 1324C-1H-1 and 1324B-7H-7 [Text S1; Fig. S2]. For our models, we assume smectite platelets have an aspect ratio (m) of 50 and a length ($m\beta$) of 0.1 μm , illite platelets have $m=20$ and $m\beta= 2 \mu\text{m}$ [Santamarina et al., 2012], and chlorite platelets have $m=25$ and $m\beta= 2.5 \mu\text{m}$ [Weber et al., 2014]. To model sample 1324C-1H-1, we simulate mudstone pore structure *NM1* consisting of 81.5% smectite and 18.5% illite. To model sample 1324B-7H-7, we simulate mudstone pore structure *NM2* consisting of 30.6% smectite, 41.7% illite, and 27.7% chlorite.

Permeability data from the constant rate-of-strain consolidation experiment on sample 1324C-1H-1 document a decrease in vertical permeability from $1.08 \times 10^{-17} \text{ m}^2$ at $\phi = 0.58$ to $5.39 \times 10^{-19} \text{ m}^2$ at $\phi = 0.46$ [Long et al., 2008]. Magnetic susceptibility analyses document a range of 0° to 15° for platelet orientations at 51.3 mbsf, corresponding to the burial depth of sample 1324C-1H-1 [Yamamoto and Sawyer, 2012]. X-ray diffraction analyses reveal that degree of preferred platelet orientation at 51 mbsf is approximately double of observations at seafloor [Day-Stirrat et al., 2012]. Additionally, Day-Stirrat et al. [2012] record an increase in preferred horizontal orientation with consolidation at IODP Site 1324. Based on this, we assume $\theta_1=0^\circ$ and $\theta_2=30^\circ$ at deposition, and θ_2 approaches 0° as compaction increases. Thus, we simulate compaction of mudstone model *NM1* with uniform representative grain orientation ($\theta = (\theta_1 + \theta_2)/2$) declining from $\theta=15^\circ$ at $\phi = 0.72$ to $\theta=0^\circ$ at $\phi = 0.32$. During compaction of *NM1* model, k_v decreases from $1.54 \times 10^{-16} \text{ m}^2$ at $\phi = 0.72$ ($\theta = 15^\circ$) to $7.09 \times 10^{-21} \text{ m}^2$ at $\phi = 0.32$ ($\theta = 0^\circ$) [Fig. 4], following a log-linear trend ($R^2=0.99$),

$$\log(k_v^{NM1}) = 10.93 \phi - 23.63 . \quad (7)$$

Simultaneously, k_h decreases from $1.39 \times 10^{-15} \text{ m}^2$ to $2.66 \times 10^{-19} \text{ m}^2$ [Table S2] and k_h/k_v increases from 8.97 to 37.59. The reduction in vertical permeability during compaction is accompanied by an increase in vertical tortuosity from 1.74 to 3.69 and a decrease in horizontal tortuosity from 1.73 to 1.47 [Table S2].

Permeability data from the constant rate-of-strain consolidation experiment on sample 1324B-7H-7 document a decrease in vertical permeability from $1.61 \times 10^{-17} \text{ m}^2$ at $\phi = 0.50$ to $3.95 \times 10^{-19} \text{ m}^2$ at $\phi = 0.33$ [Long et al., 2008]. Magnetic susceptibility analyses document a range of 0° to 12° for platelet orientations at 60.6 mbsf, corresponding to the burial depth of sample 1324B-7H-7 [Yamamoto and Sawyer, 2012]. X-ray diffraction analyses reveal that degree of preferred platelet at 60.6 mbsf is approximately double of observations at seafloor [Day-Stirrat et al., 2012]. Since horizontal bedding orientation increases with consolidation at IODP Site 1324 [Day-Stirrat et al., 2012], we assume $\theta_1 = 0^\circ$ and $\theta_2 = 24^\circ$ at deposition, and θ_2 approaches 0° as compaction is simulated. Thus, we simulate compaction of mudstone model *NM2* with uniform representative grain orientation ($\theta = (\theta_1 + \theta_2)/2$) decreasing from $\theta = 12^\circ$ at $\phi = 0.58$ to $\theta = 0^\circ$ at $\phi = 0.25$. During compaction of *NM2* model, k_v decreases from $3.11 \times 10^{-17} \text{ m}^2$ at $\phi = 0.58$ ($\theta = 12^\circ$) to $4.79 \times 10^{-20} \text{ m}^2$ at $\phi = 0.25$ ($\theta = 0^\circ$) [Fig. 4], following a log-linear trend ($R^2 = 0.99$),

$$\log(k_v^{NM2}) = 8.28 \phi - 21.32 . \quad (8)$$

Simultaneously, k_h decreases from $2.27 \times 10^{-16} \text{ m}^2$ to $1.51 \times 10^{-18} \text{ m}^2$ [Table S2] and k_h/k_v increases from 7.29 to 31.6. The reduction in vertical permeability during compaction is accompanied by an increase in vertical tortuosity from 1.29 to 3.66 and a decrease in horizontal tortuosity from 2.23 to 1.47 [Table S2]. Our modeled porosity-permeability trends for *NM1* and *NM2* shows good agreement with experimental consolidation datasets ($R^2 = 0.78$ and 0.74). In particular, the slopes of porosity-log permeability trends described by models *NM1* and *NM2* (Eq. 7 and Eq. 8 respectively) are very similar to the experimental trends described by Long et al. [2008] [Fig. 4].

Over $\phi = 0.46 - 0.58$, Eq. 7 underestimates the permeability of sample 1324C-1H-1. While model *NM1* is simulated using clay platelets, sample 1324C-1H-1 also has 15 wt.% quartz, 8.6 wt.% plagioclase, and 6.0 wt.% calcite [Day-Stirrat et al., 2012]. Similarly, over $\phi = 0.33 - 0.50$, Eq. 8 underestimates the permeability of sample 1324B-7H-7. While model *NM2* is simulated using clay platelets, sample 1324B-7H-7 also contains 17 wt.% quartz, 9.2 wt.% plagioclase, and 4.8 wt.% calcite [John and Adatte, 2009]. Our modeled results predict lower permeability of natural samples as they do not account for the presence

of sand, silt and marl, which have been shown to have a permeability-enhancing effect in mudstones [Yang and Aplin, 2010; Dewhurst et al., 1999a; Schneider et al., 2011]. However, over $\phi=0.25-0.72$ our model results exhibit good capability to predict the permeability of natural mudstones with high clay weight fraction. In addition to simulating experimental values of vertical permeability, our models also provide an estimate of horizontal permeability, permeability anisotropy, and tortuosity. Thus, our methodology of simulating flow through mudstone pore structures provides a simple way to make first-order predictions of mudstone permeability based on clay composition and dimensions. We extend the developed methodology to understand the evolution of permeability during fluid injection in compacted mudstones.

5. Permeability During Fluid Injection

5.1. Modeling Fluid Injection in Mudstones

Anthropogenic activities such as wastewater disposal, hydraulic fracturing, and carbon sequestration involve injection of large fluid volumes into the subsurface, which can increase vertical mudstone permeability by several orders of magnitude [Soeder, 1988]. The increase in vertical permeability from fluid injection has been attributed to the growth of microfracture networks [Slatt and O'Brien, 2011] and propagation of macrofractures [Mayerhofer et al., 2006]. We extend our methodology to understand the permeability response of compacted mudstone systems to fluid injection. The compacted, intermediate mudstone with $\phi=0.07$ and k_v of $1.02 \times 10^{-20} \text{ m}^2$ ($\theta=0^\circ$), is used as the starting model for fluid injection simulations. Using lattice Boltzmann simulations, we calculate evolution of vertical permeability for (a) growth of microfracture network [Fig. 5a] where we simulate preferential dilation of intrabed pores during fluid injection [Table S3] and (b) macrofracture propagation [Fig. 5b] where we simulate the increase in macrofracture width during fluid injection [Table S4]. Following the approach we employed in our compaction analysis, we also evaluate the log-linear relationship between vertical permeability and porosity in mudstones during fluid injection.

5.2. Permeability Evolution upon Fluid Injection

As interbed pore throats (ε^{mf}) [Fig. 5a] increase from 11.42 nm to 1154 nm in the microfracture network model, vertical permeability (k_v^{mf}) increases from $1.02 \times 10^{-20} \text{ m}^2$ at $\phi = 0.07$ to $9.59 \times 10^{-15} \text{ m}^2$ at $\phi = 0.57$ [Fig. 6], following the trend ($R^2 = 0.88$),

$$\log(k_v^{mf}) = 10.79 \phi - 19.38. \quad (9)$$

This vertical permeability increase is accompanied by a decrease in vertical tortuosity from 2.2 to 1 [Fig. S1b].

As the macrofracture width (ε^{frac}) [Fig. 5b] increases from 11.42 nm to 6297 nm, vertical permeability (k_v^{frac}) increases from $1.02 \times 10^{-20} \text{ m}^2$ at $\phi = 0.07$ to $3.85 \times 10^{-14} \text{ m}^2$ at $\phi = 0.55$ [Fig. 6], following the trend ($R^2 = 0.93$),

$$\log(k_v^{frac}) = 16.87 \phi - 21.5. \quad (10)$$

This vertical permeability increase is accompanied by a decline in vertical tortuosity from 2.2 to 1 [Fig. S1b].

5.3. Comparison of Permeability Evolution in Fluid Injection Models

To compare the relative contribution of fracture flow to increases in mudstone permeability, we calculate the effective fracture width at each step of simulated fluid injection. Effective fracture width for growth of microfracture network (ε_{eff}^{mf}) and macrofracture propagation (ε_{eff}^{frac}) are calculated as

$$\varepsilon_{eff}^{mf} = n^{mf} * \varepsilon^{mf} - \varepsilon^i, \quad (11)$$

$$\varepsilon_{eff}^{frac} = \varepsilon^{frac} - \varepsilon^i, \quad (12)$$

where n^{mf} is the number of microfractures simulated in our model ($n^{mf}=3$) and ε^i is the pore throat width of the starting model ($\varepsilon^i=11.42 \text{ nm}$).

Over $\phi=0.10-0.36$, we calculate greater values of k_v^{mf} than k_v^{frac} [Fig. 6]. Simultaneously, ε_{eff}^{mf} increases from 137 nm to 1370 nm [Table S3], ε_{eff}^{frac} increases from 366 nm to 2780 nm [Table S4] and we calculate $\tau_v^{mf} < \tau_v^{frac}$ [Fig. S1b]. This indicates that the growth of a distributed microfracture network results in smaller vertical tortuosity despite lower effective fracture width compared to a single macrofracture. The lower values of vertical tortuosity associated with growth of a microfracture network compared to macrofracture propagation result in $k_v^{mf} > k_v^{frac}$. Over $\phi=0.36-0.41$, we calculate greater values of k_v^{frac} than k_v^{mf} [Fig. 6]. Simultaneously, ε_{eff}^{mf} increases from 1370 nm to 1890 nm [Table S3], ε_{eff}^{frac} increases from 2780 nm to 3430 nm [Table S4] and we calculate $\tau_v^{frac} < \tau_v^{mf}$ [Fig. S1b]. The crossover of vertical permeability trends k_v^{mf} and k_v^{frac} [Fig. 6] coincides with tortuosity in the macrofracture model becoming lower than tortuosity in the microfracture network [Fig. S1b]. Over $\phi=0.41-0.57$, we calculate greater values of k_v^{frac} than k_v^{mf} and the rate of increase in vertical permeability with respect to porosity declines in both models [Fig. 6]. Simultaneously, ε_{eff}^{mf} increases from 1890 nm to 3430 nm [Table S3], ε_{eff}^{frac} increases from 3430 nm to 6290 nm [Table S4] and we calculate $\tau_v^{frac} \approx \tau_v^{mf} \approx 1$.

Our models suggest that upon initial fluid injection in low porosity mudstones, the growth of a distributed microfracture network yields a greater vertical mudstone permeability compared to propagation of a macrofracture. This is consistent with several experimental, numerical, and field scale studies that record greater increase in mudstone permeability upon distributed fracture growth compared to a wide macrofracture [Backeberg et al., 2017; Matthäi and Belayneh, 2004; Dahl et al., 2015]. Recent studies show that productivity of shale gas wells increases with the use of micro-proppants (1-50 μm) compared to typical proppants (100-300 μm) due to greater permeability enhancement provided by microfractures of smaller width [Calvin et al., 2017]. Our models show that the growth of a distributed microfracture network results in faster decrease in tortuosity of the representative mudstone volume despite lower effective fracture width compared to a single macrofracture.

Our results indicate that as porosity increases upon fluid injection, the macrofracture yields greater vertical mudstone permeability than a microfracture network as the macrofracture becomes wide enough to conduct the bulk of fluid flux. However, wide fractures resulting in representative mudstone volume porosities greater than 0.3 are not observed in the subsurface due to high fracture opening pressures [Fisher et al., 2002]. Our results suggest that over realistic porosities in compacted mudstones ($\phi < 0.3$) the growth of a distributed microfracture network yields greater permeability increase than a single macrofracture. Thus, our modeling approach can be used to understand mudstone permeability response to fracture geometries. This predictive capability can help design injection strategies during anthropogenic activities such as hydraulic fracturing, wastewater disposal, and carbon sequestration.

5. Conclusions

We develop a simple model that predicts mudstone permeability by simulating fluid flow through pore structures using the lattice Boltzman method. We validate our model against porosity-permeability observations and extend the methodology to predict how permeability changes during fluid injection. Our model represents mudstones as an assemblage of cuboidal grains with thickness (β), aspect ratio (m), orientation (θ) and with intrabed (ϵ) and interbed (λ) pore widths. Compaction models for three homogenous mudstones spanning the representative range of clay platelet lengths (0.1 – 3 μm) and aspect ratios (20-50) document a variation in mudstone permeability of over 3 orders of magnitude. Compaction of homogenous smectite and kaolinite models document log-linear declines in vertical permeability from $8.31 \times 10^{-15} \text{ m}^2$ – $6.84 \times 10^{-17} \text{ m}^2$ at $\phi = 0.73 - 0.80$ to $6.33 \times 10^{-19} \text{ m}^2$ - $1.30 \times 10^{-23} \text{ m}^2$ at $\phi = 0.14 - 0.16$, showing good correlation with experimental datasets ($R^2 = 0.42$ and $R^2 = 0.56$). Additionally, modeled trends of permeability and tortuosity from compaction of homogenous mudstone models lie within range of experimentally observed values on natural mudstones. We advance our validated methodology to predict the porosity-permeability character of natural mudstones consisting of smectite, illite and chlorite platelets. Over porosity of 0.32-0.58, the porosity-permeability trends described by our heterogenous

mudstone models replicating the mineralogical composition of natural mudstones (models *NM1* and *NM2*) show good correlation with experimental datasets ($R^2=0.78$ and $R^2=0.74$). We extend our methodology to permeability during fluid injection in compacted mudstone due to (1) growth of a microfracture network where k_v increases from $1.02 \times 10^{-20} \text{ m}^2$ at $\phi = 0.07$ to $9.59 \times 10^{-15} \text{ m}^2$ at $\phi = 0.57$ and to (2) propagation of a macrofracture where k_v increases from $1.02 \times 10^{-20} \text{ m}^2$ at $\phi = 0.07$ to $3.84 \times 10^{-15} \text{ m}^2$ at $\phi = 0.55$. We document that a distributed microfracture network results in greater mudstone permeability at lower mudstone porosities ($0.07 - 0.36$) despite lower effective fracture width, whereas a macrofracture yields greater permeability at higher porosity ($0.36 - 0.57$) once the macrofracture becomes wide enough to conduct the bulk of the fluid flux. In conclusion, we develop an approach to simulate mudstone permeability during compaction or fluid injection using a simple inputs of clay platelet type (mineralogy), platelet geometry (thickness and aspect ratio) and pore throats (porosity). Thus, our model can be used to evaluate fluid flow in mudstone during geological processes or anthropogenic activities.

Acknowledgements: This work has been funded in part by fellowships to Harsh Biren Vora from the Department of Earth, Environment and Planetary Science, Rice University. Computing facilities were made available through the Center for Computational Geophysics. The authors benefitted from discussions on numerical modeling with Dr. Julia Morgan. Modeling results and information can be obtained in supporting information and at https://figshare.com/projects/LBM_Mudstone_k/58655.

References

- Aplin, A. C., I. F. Matenaar, D. K. McCarty, and B. A. van der Pluijm (2006), Influence of mechanical compaction and clay mineral diagenesis on the microfabric and pore-scale properties of deep-water Gulf of Mexico mudstones, *Clays Clay Miner.*, 54(4), 500–514, doi:10.1346/CCMN.2006.0540411.
- Aplin, A. C., Matenaar, I. F., & van der Pluijm, B. (2003). Influence of mechanical compaction and chemical diagenesis on the microfabric and fluid flow properties of Gulf of Mexico mudstones. *Journal of Geochemical Exploration*, 78, 449–451
- Arch, J., & Maltman, A. (1990). Anisotropic permeability and tortuosity in deformed wet sediments. *Journal of Geophysical Research: Solid Earth*, 95(B6), 9035–9045.
- Backeberg, N. R., F. Iacoviello, M. Rittner, T. M. Mitchell, A. P. Jones, R. Day, J. Wheeler, P. R. Shearing, P. Vermeesch, and A. Striolo (2017), Quantifying the anisotropy and tortuosity of permeable pathways in clay-rich mudstones using models based on X-ray tomography, *Sci. Rep.*, 7(1), 1–12, doi:10.1038/s41598-017-14810-1.
- Bennett, R. H., Fischer, K. M., Lavoie, D. L., Bryant, W. R., & Rezac, R. (1989). Porometry and fabric of marine clay and carbonate sediments: determinants of permeability. *Marine Geology*, 89(1-2), 127–152.
- Bhandari, A. R., P. B. Flemings, P. J. Polito, M. B. Cronin, and S. L. Bryant (2015), Anisotropy and Stress Dependence of Permeability in the Barnett Shale, *Transp. Porous Media*, 108(2), 393–411, doi:10.1007/s11242-015-0482-0.
- Bolton, A. J., A. J. Maltman, and Q. Fisher (2000), Anisotropic permeability and bimodal pore-size distributions of fine-grained marine sediments, *Mar. Petrol. Geol.*, 17, 657–672.
- Bosl, W. J., J. Dvorkin, and A. Nur (1998), A study of porosity and permeability using a lattice Boltzmann simulation, *Geophys. Res. Lett.*, 25(9), 1475–1478, doi:10.1029/98gl00859.
- Boudreau, B. P., and F. J. R. Meysman (2006), Predicted tortuosity of muds, *Geology*, 34(8), 693–696, doi:10.1130/G22771.1.
- Bouzidi, M., M. Firdaouss, and P. Lallemand (2001), Momentum transfer of a Boltzmann-lattice fluid with boundaries, *Phys. Fluids*, 13(11), 3452–3459, doi:10.1063/1.1399290.
- Bowers, G. L., and T. J. Katsube (2002), The Role of Shale Pore Structure on the Sensitivity of Wire-Line Logs to Overpressure, *Press. Regimes Sediment. Basins Their Predict. AAPG Mem.* 76, 43–60.
- Calvin, J., B. Grieser, and T. Bachman (2017), Enhancement of Well Production in the SCOOP Woodford Shale through the Application of Microproppant, *SPE Hydraul. Fract. Technol. Conf. Exhib.*, doi:10.2118/184863-MS.
- Carman, P. C. (1937). Fluid flow through granular beds. *Trans. Inst. Chem. Eng.*, 15, 150–166.

403 Chukwudozie, C. P. (2011). Pore-scale Lattice Boltzmann simulations of inertial flows in realistic porous
404 media: a first principle analysis of the forchheimer relationship.

405 Clennell, M. B., D. N. Dewhurst, K. M. Brown, and G. K. Westbrook (1999), Permeability anisotropy of
406 consolidated clays, *Muds Mudstones Phys. Fluid Flow Prop.*, 158, 79–96,
407 doi:10.1144/GSL.SP.1999.158.01.07.

408 Cook, A. E., and D. E. Sawyer (2015), The mud-sand crossover on marine seismic data, *Geophysics*,
409 80(6), A109–A114, doi:10.1190/geo2015-0291.1.

410 Dahl, J., P. Nguyen, R. Dusterhoft, J. Calvin, and S. Siddiqui (2015), Application of micro-proppant to
411 enhance well production in unconventional reservoirs: Laboratory and field results, *SPE West. Reg.*
412 *Meet. 2015 Old Horizons, New Horizons Through Enabling Technol., 2015–Janua*, 923–946.

413 Daigle, H., and B. Dugan (2011), Permeability anisotropy and fabric development: A mechanistic
414 explanation, *Water Resour. Res.*, 47(12), 1–11, doi:10.1029/2011WR011110.

415 Daigle, H., and E. J. Screaton (2016), Evolution of sediment permeability during burial and subduction,
416 *Crustal Permeability*, 104–121, doi:10.1002/9781119166573.ch11.

417 Day-Stirrat, R. J., A. C. Aplin, J. Środoń, and B. A. van der Pluijm (2008), Diagenetic reorientation of
418 phyllosilicate minerals in Paleogene mudstones of the Podhale Basin, southern Poland, *Clays Clay*
419 *Miner.*, 56(1), 100–111, doi:10.1346/CCMN.2008.0560109.

420 Day-Stirrat, R. J., P. B. Flemings, Y. You, A. C. Aplin, and B. A. van der Pluijm (2012), The fabric of
421 consolidation in Gulf of Mexico mudstones, *Mar. Geol.*, 295–298, 77–85,
422 doi:10.1016/j.margeo.2011.12.003.

423 Deamer, G. A., & Kodama, K. P. (1990). Compaction-induced inclination shallowing in synthetic and
424 natural clay-rich sediments. *Journal of Geophysical Research: Solid Earth*, 95(B4), 4511–4529.

425 Dewhurst, D. N., A. C. Aplin, and J.-P. Sarda (1999b), Influence of clay fraction on pore-scale properties
426 and hydraulic conductivity of experimentally compacted mudstones, *J. Geophys. Res.*, 104, 29261,
427 doi:10.1029/1999JB900276.

428 Dewhurst, D. N., K. M. Brown, M. B. Clennell, and G. K. Westbrook (1996), A comparison of the fabric
429 and permeability anisotropy of consolidated and sheared silty clay, *Eng. Geol.*, 42(4), 253–267,
430 doi:10.1016/0013-7952(95)00089-5.

431 Dewhurst, D. N., Y. Yang, and a. C. Aplin (1999a), Permeability and fluid flow in natural mudstones,
432 *Geol. Soc. London, Spec. Publ.*, 158(1), 23–43, doi:10.1144/GSL.SP.1999.158.01.03.

433 Dugan, B. (2000), Overpressure and Fluid Flow in the New Jersey Continental Slope: Implications for
434 Slope Failure and Cold Seeps, *Science (80-)*, 289(5477), 288–291,
435 doi:10.1126/science.289.5477.288.

436 England, W. A., A. S. Mackenzie, D. M. Mann, and T. M. Quigley (1987), The movement and
437 entrapment of petroleum fluids in the subsurface, *J. Geol. Soc. London.*, 144(2), 327–347,
438 doi:10.1144/gsjgs.144.2.0327.

439 Fisher, M. K., C. A. Wright, B. M. Davidson, A. K. Goodwin, E. O. Fielder, W. S. Buckler, and N. P.
440 Steinsberger (2002), Integrating Fracture Mapping Technologies to Optimize Stimulations in the
441 Barnett Shale, *SPE Annu. Tech. Conf. Exhib.*, doi:10.2118/77441-MS.

442 Freeze, R. A., and J. A. Cherry (1979), Groundwater, Prentice Hall, Englewood Cliffs, N. J.

443 Garven, G., and R. A. Freeze (1984), Theoretical analysis of the role of groundwater flow in the genesis
444 of stratabound ore deposits. 2: Quantitative results, *Am. J. Sci.*, 284, 1125–1174.

445 Heath, J. E. (2010), Multi-scale petrography and fluid dynamics of caprocks associated with geological
446 CO₂ storage, *Dep. Earth Environ. Sci., PhD* (December), 437.

447 Iversen, N., and B. B. Jorgensen (1993), Diffusion coefficients of sulfate and methane in marine
448 sediment: Influence of porosity, *Geochim. Cosmochim. Acta*, 57(5), 571–578.

449 John, C. M., and T. Adatte (2009), Data report : X-ray analyses of bulk sediment in IODP Holes U1320A
450 and U1324B , northern Gulf of Mexico, 308, doi:10.2204/iodp.proc.308.214.2009.

451 Katsube, T. J., & Williamson, M. A. (1994). Effects of diagenesis on shale nano-pore structure and
452 implications for sealing capacity. *Clay minerals*, 29(4), 451-461.

453 Keehm, Y. (2004), Permeability prediction from thin sections: 3D reconstruction and Lattice-Boltzmann
454 flow simulation, *Geophys. Res. Lett.*, 31(4), 3–6, doi:10.1029/2003GL018761.

455 Kozeny, J. (1927). Über kapillare leitung der wasser in boden. *Royal Academy of Science, Vienna, Proc.*
456 *Class I*, 136, 271-306.

457 Kuila, U., and M. Prasad (2013), Specific surface area and pore-size distribution in clays and shales,
458 *Geophys. Prospect.*, 61(2), 341–362, doi:10.1111/1365-2478.12028.

459 Latt, J. (2008), Choice of units in lattice Boltzmann simulations, *Lattice Boltzmann How tos*, (April), 1–6.

460 Long, H., P. B. Flemings, J. T. Germaine, D. M. Saffer, and B. Dugan (2008), Data report: Consolidation
461 characteristics of sediments from IODP Expedition 308, Ursa Basin, Gulf of Mexico, *Proc. Integr.*
462 *Ocean Drill. Progr. Sci. Results*, 308, doi:10.2204/iodp.proc.308.204.2008.

463 Loucks, R. G., R. M. Reed, S. C. Ruppel, and D. M. Jarvie (2009), Morphology, Genesis, and
464 Distribution of Nanometer-Scale Pores in Siliceous Mudstones of the Mississippian Barnett Shale, *J.*
465 *Sediment. Res.*, 79(12), 848–861, doi:10.2110/jsr.2009.092.

466 Lucia, F. J., Jennings Jr, J. W., Rahnis, M., & Meyer, F. O. (2001). Permeability and rock fabric from
467 wireline logs, Arab-D reservoir, Ghawar field, Saudi Arabia. *GeoArabia*, 6(4), 619-646.

468 Matthäi, S. K., and M. Belayneh (2004), Fluid flow partitioning between fractures and a permeable rock
469 matrix, *Geophys. Res. Lett.*, 31(7), 1–5, doi:10.1029/2003GL019027.

470 Mayerhofer, M. J., E. P. Lolon, J. E. Youngblood, and J. R. Heinze (2006), Integration of Microseismic-
471 Fracture-Mapping Results with Numerical Fracture Network Production Modeling in the Barnett
472 Shale, *SPE Annu. Tech. Conf. Exhib.*, doi:10.2118/102103-MS.

473 Mitchell, J. K., & Soga, K. (2005). *Fundamentals of soil behavior* (Vol. 3). New York: John Wiley &
474 Sons.

475 Mondol, N. H., Bjørlykke, K., & Jahren, J. (2008). Experimental compaction of clays: Relationship
476 between permeability and petrophysical properties in mudstones. *Petroleum Geoscience*, 14(4), 319-
477 337.

478 Mondol, N. H., K. Bjørlykke, J. Jahren, and K. Høeg (2007), Experimental mechanical compaction of
479 clay mineral aggregates-Changes in physical properties of mudstones during burial, *Mar. Pet. Geol.*,
480 24(5), 289–311, doi:10.1016/j.marpetgeo.2007.03.006.

481 Nabovati, A., and A. C. M. Sousa (2007), Fluid Flow Simulation in Random Porous Media at Pore Level
482 Using the Lattice Boltzmann Method, *J. Eng. Sci. Technol.*, 2(3), 226–237, doi:10.1007/978-3-540-
483 75995-9_172.

484 Nagaraj, T. S. (1994). Stress state permeability relationships for overconsolidated clays. *Geotechnique*,
485 44(2), 349-352.

486 Neuzil, C. E. (1994). How permeable are clays and shales?. *Water resources research*, 30(2), 145-150.

487 Olsen, H. W. (1960), Hydraulic Flow Through Saturated Clays, *Clays Clay Miner.*, 9(1), 131–161,
488 doi:10.1346/CCMN.1960.0090108.

489 Rose, H. E. (1945). An investigation into the laws of flow of fluids through beds of granular materials.
490 *Proceedings of the Institution of Mechanical Engineers*, 153(1), 141-148.

491 Santamarina, J. C., K. A. Klein, Y. H. Wang, and E. Prencke (2002), Specific surface: determination and
492 relevance, *Can. Geotech. J.*, 39(1), 233–241, doi:10.1139/t01-077.

493 Sawyer, D. E., R. Jacoby, P. Flemings, and J. T. Germaine (2008), Data report : particle size analysis of
494 sediments in the Ursa Basin , IODP Expedition 308 Sites U1324 and U1322 , northern Gulf of
495 Mexico, 308, 1–20, doi:10.2204/iodp.proc.308.205.2008.

496 Schneider, J., P. B. Flemings, R. J. Day-Stirrat, and J. T. Germaine (2011), Insights into pore-scale
497 controls on mudstone permeability through resedimentation experiments, *Geology*, 39(11), 1011–
498 1014, doi:10.1130/G32475.1.

499 Schwartz, L. M., and J. R. Banavar (1989), Transport properties of disordered continuum systems, *Phys.*
500 *Rev. B*, 39(16), 11965–11970, doi:10.1103/PhysRevB.39.11965.

501 Slatt, R. M., and N. R. O'Brien (2011), Pore types in the Barnett and Woodford gas shales: Contribution
502 to understanding gas storage and migration pathways in fine-grained rocks, *Am. Assoc. Pet. Geol.*
503 *Bull.*, 95(12), 2017–2030, doi:10.1306/03301110145.

504 Soeder, D. J. (1988). Porosity and permeability of eastern Devonian gas shale. *SPE Formation*
505 *Evaluation*, 3(01), 116-124.

- 506 Weber, C., M. Heuser, and H. Stanjek (2014), A collection of aspect ratios of common clay minerals
507 determined from conductometric titrations, *Clay Miner.*, 49(3), 495–498,
508 doi:10.1180/claymin.2014.049.3.10.
- 509 Xiaorong Luo, and G. Vasseur (1992), Contributions of compaction and aquathermal pressuring to
510 geopressure and the influence of environmental conditions, *Am. Assoc. Pet. Geol. Bull.*, 76(10),
511 1550–1559, doi:10.1306/BDF8FB0-1718-11D7-8645000102C1865D.
- 512 Yamamoto, Y., & Sawyer, D. E. (2012). Systematic Spatial Variations in the Fabric and Physical
513 Properties of Mass-Transport Deposits in the Ursa Region, Northern Gulf of Mexico. In *Submarine*
514 *Mass Movements and Their Consequences* (pp. 649-658). Springer, Dordrecht.
- 515 Yang, Y., and A. C. Aplin (1998), Influence of lithology and compaction on the pore size distribution and
516 modelled permeability of some mudstones from the Norwegian margin, *Mar. Pet. Geol.*, 15(2), 163–
517 175, doi:10.1016/S0264-8172(98)00008-7.
- 518 Yang, Y., and A. C. Aplin (2007), Permeability and petrophysical properties of 30 natural mudstones, *J.*
519 *Geophys. Res. Solid Earth*, 112(3), doi:10.1029/2005JB004243.
- 520 Yang, Y., and A. C. Aplin (2010), A permeability-porosity relationship for mudstones, *Mar. Pet. Geol.*,
521 27(8), 1692–1697, doi:10.1016/j.marpetgeo.2009.07.001.

Table 1: Clay mineralogy of reference samples for mudstone porosity-permeability behavior. Data from Long et al. [2008], Sawyer et al. [2009] and Day-Stirrat et al. [2012].

| | Sample: 1324C-1H-1 | Sample: 1324b-7H-7 |
|--------------------------------------|---------------------------|---------------------------|
| Core Top (mbsf) | 51.1 | 60.3 |
| Initial Porosity | 0.59 | 0.51 |
| Clay Mineral Fraction (wt. %) | 70.4 | 68.9 |
| Smectite (wt. %) | 82.1 | 27.3 |
| Illite (wt. %) | 17.9 | 38.8 |
| Chlorite (wt. %) | Trace | 25.0 |
| Quartz (wt. %) | Trace | 8.8 |
| Consolidation Experiment | CRS 799 | CRS 015B |

Figure Captions

Figure 1: (a) Schematic of initial mudstone structure built from clay platelets (grey cuboids) using inputs of platelet thickness (β) and aspect ratio (m) and intrabed (ε) and interbed (λ) pore throat widths and orientation angle with respect to horizontal (θ). Flux of fluid in vertical and horizontal direction are represented by q_v and q_h respectively. (b) Mudstone structure after compaction simulated by reduction in pore throat widths, ε and λ , and platelet orientation angle (θ).

Figure 2: Porosity-vertical permeability model results (symbols) and best-fit lines during compaction for kaolinite, smectite, and intermediate mudstone models. Modeled porosity-permeability trends show good correlation with natural and experimental mudstone permeability compilation [Neuzil, 1994] and experimental data on kaolinite and smectite [Mondol et al., 2008].

Figure 3: Permeability anisotropy (k_h/k_v) exhibits an inverse correlation with porosity (ϕ) and platelet size ($m\beta$) during compaction of kaolinite, smectite and intermediate mudstone models.

Figure 4: Porosity-permeability predictions (symbols) and best-fit lines during compaction of heterogenous mudstone models *NM1* (replicating mineralogy of sample 1324C-1H-1) and *NM2* (replicating mineralogy of sample 1324B-7H-7). Modeled porosity-permeability trends of *NM1* and *NM2* lie within range of mudstone permeability compilation [Neuzil, 1994], and show good correlation with experimental data on natural mudstones 1324C-1H-1 (Experiment CRS799) and 1324B-7H-7 (Experiment CRS015B) respectively [Long et al., 2008].

Figure 5: (a) Schematic of a microfracture network in compacted intermediate mudstone model during fluid injection. In our model microfracture width increases from 11.42 nm to 1154 nm [Table S3] (b) Schematic of macrofracture through compacted intermediate mudstone model during fluid injection. In our model, macrofracture width increases from 11.42 nm to 6297 nm [Table S4].

Figure 6: Porosity-vertical permeability model predictions (symbols) and best-fit lines during fluid injection accommodated through prescribed growth of microfracture network or propagation of a macrofracture. Upto $\phi=0.36$, growth of microfracture network (k_v^{mf}) results in greater permeability

increase than macrofracture propagation (k_v^{frac}). Beyond $\phi=0.37$, $k_v^{frac} > k_v^{mf}$ as the macrofracture becomes wide enough to conduct the bulk of fluid flux. Mudstone permeability compilation [Neuzil, 1994] shown for reference.

Figure 1.

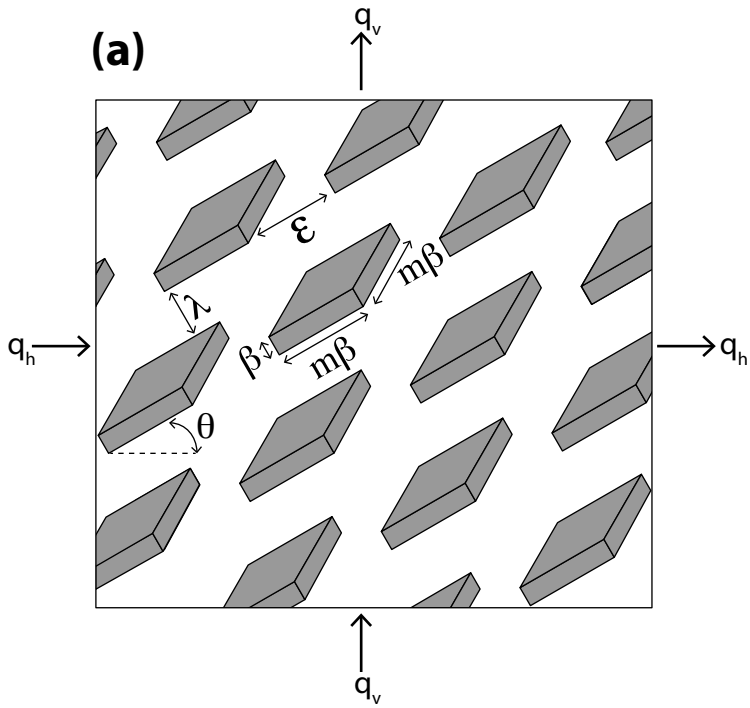
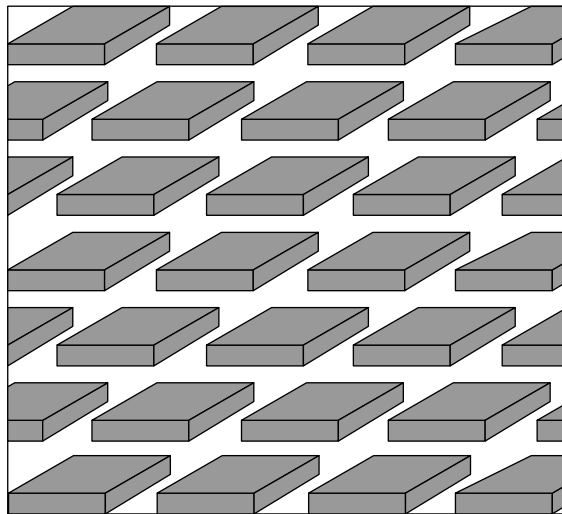
(a)**(b)**

Figure 2.

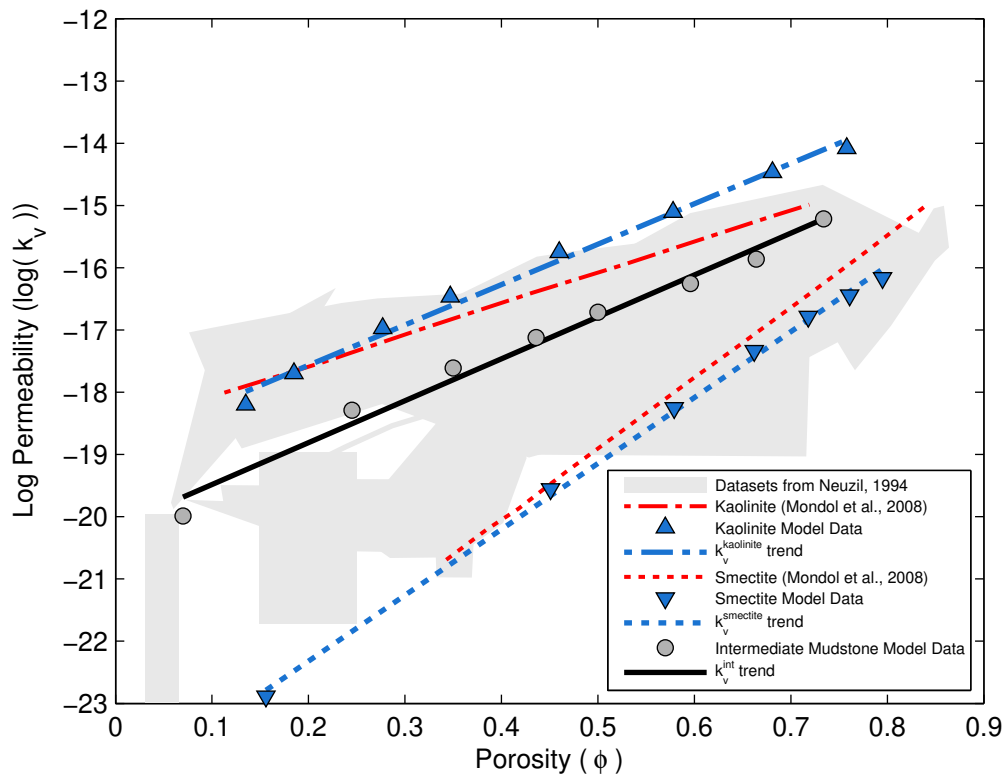


Figure 3.

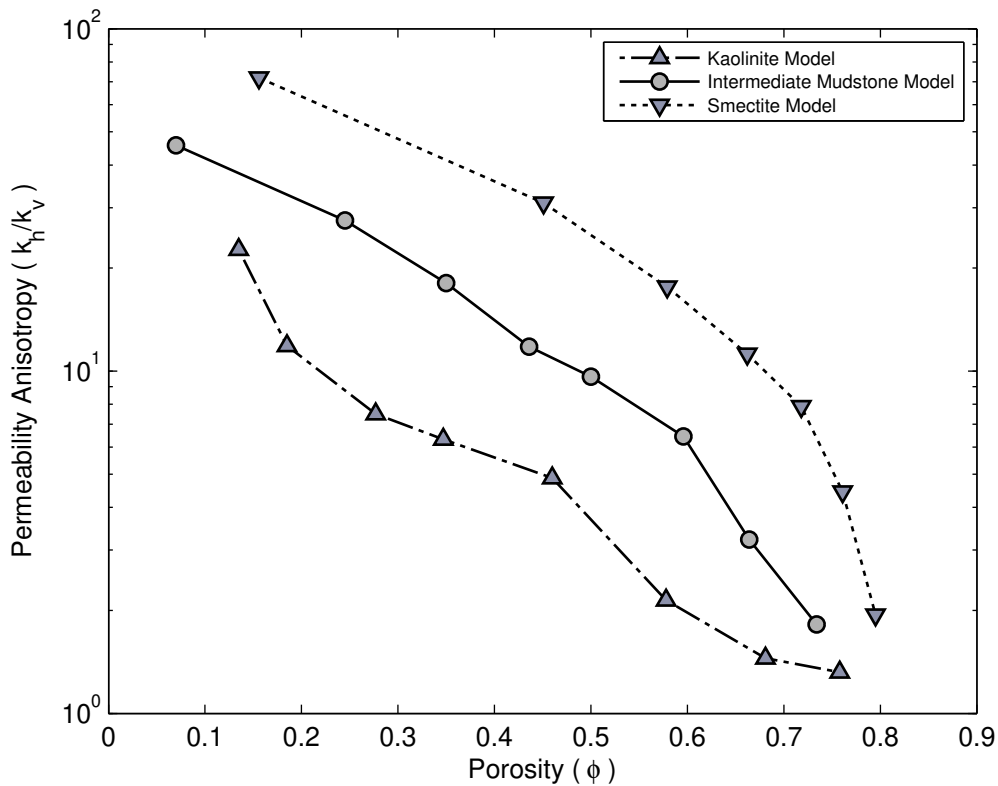


Figure 4.

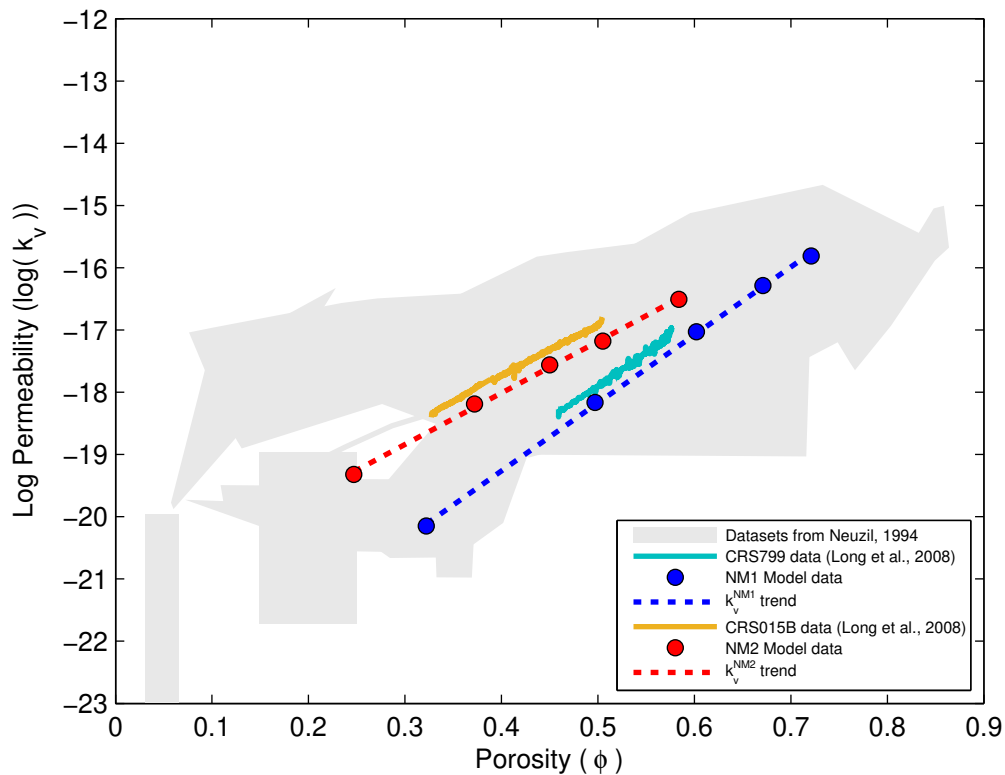


Figure 5.

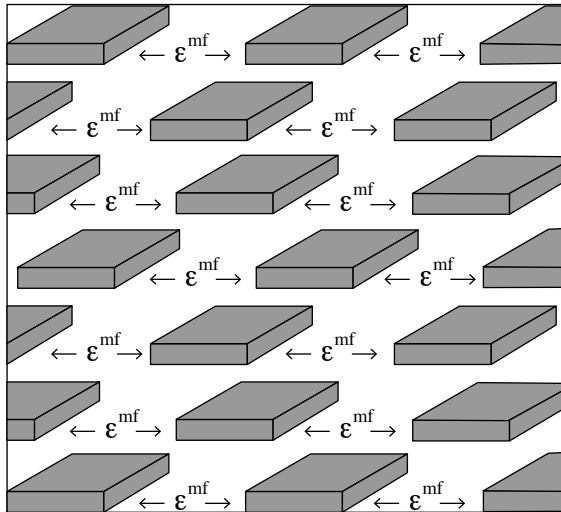
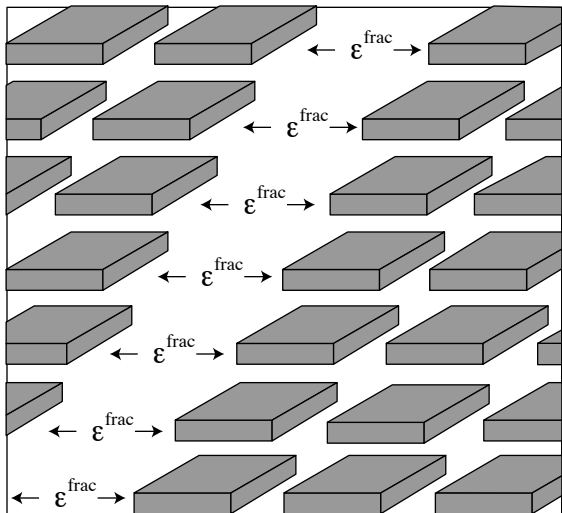
(a)**(b)**

Figure 6.

